Featured in Physics

# A room temperature polar magnetic metal

Hongrui Zhang,[1,*,†] Yu-Tsun Shao,[2,*] Rui Chen,[1,3,*] Xiang Chen,[3,4,*] Sandhya Susarla,[1,3] David Raftrey,[3,5] Jonathan T. Reichanadter,[4,6] Lucas Caretta,[1] Xiaoxi Huang,[1] Nicholas S. Settineri,[6] Zhen Chen,[2] Jingcheng Zhou,[1] Edith Bourret-Courchesne,[3] Peter Ercius,[7] Jie Yao,[1,3] Peter Fischer,[3,5] Jeffrey B. Neaton,[3,4,8] David A. Muller,[2,9] Robert J. Birgeneau,[3,4] and Ramamoorthy Ramesh[1,3,4,‡]

[1]*Department of Materials Science and Engineering, University of California, Berkeley, California 94720, USA*
[2]*School of Applied and Engineering Physics, Cornell University, Ithaca, New York 14850, USA*
[3]*Materials Sciences Division, Lawrence Berkeley National Lab, Berkeley, California 94720, USA*
[4]*Department of Physics, University of California, Berkeley, California 94720, USA*
[5]*Physics Department, UC Santa Cruz, Santa Cruz, California 95064, USA*
[6]*Department of Electrical Engineering, University of California, Berkeley, California 94720, USA*
[7]*The Molecular Foundry, Lawrence Berkeley National Laboratory, Berkeley, California 94720, USA*
[8]*Kavli Energy Nanosciences Institute at Berkeley, Berkeley, California 94720, USA*
[9]*Kavli Institute at Cornell for Nanoscale Science, Cornell University, Ithaca, New York 14850, USA*

(Received 16 October 2021; accepted 8 March 2022; published 6 April 2022)

The emergence of long-range magnetic order in noncentrosymmetric compounds has stimulated interest in the possibility of exotic spin transport phenomena and topologically protected spin textures for applications in next-generation spintronics. Polar magnets, with broken symmetries of spatial inversion and time reversal, usually host chiral spin textures. This work reports on a wurtzite-structure polar magnetic metal, identified as $AA'$-stacked $(Fe_{0.5}Co_{0.5})_5GeTe_2$, which exhibits a Néel-type skyrmion lattice as well as a Rashba-Edelstein effect at room temperature. Atomic resolution imaging of the structure reveals a structural transition as a function of Co-substitution, leading to the emergence of the polar phase at 50% Co. This discovery reveals an unprecedented layered polar magnetic system for investigating intriguing spin topologies, and it ushers in a promising new framework for spintronics.

DOI: 10.1103/PhysRevMaterials.6.044403

Noncentrosymmetric magnets offer an extraordinary platform for exploring fascinating magnetic, quantum topological phases, due to broken crystal symmetries [1–7]. As an example, magnetic skyrmions [8–10] have been observed in polar magnets and are usually stabilized by an antisymmetric Dzyaloshinskii-Moriya interaction (DMI). In polar magnets such as $GaV_4S_8$ ($C_{3v}$) [11], $VOSe_2O_5$ ($C_{4v}$) [12], $GaV_4Se_8$ ($C_{3v}$) [13], and PtMnGa ($C_{3v}$) [14] with $C_{nv}$ crystal symmetry, the DMI confines the magnetic modulation direction vector to be perpendicular to the polar axis. Thus, a Néel-type skyrmion lattice is stable once a suitable magnetic field is applied along the polar axis. In addition, in polar metals or semiconductors [15,16], the crystal structure leads to a built-in electric potential along the polar axis and spin-orbit interaction, which is the essence of the Rashba effect [17]. The Rashba Hamiltonian can be expressed as $H_R = \alpha_R(\vec{k} \times \vec{\sigma}) \cdot \vec{z}$, where $\alpha_R$ is the Rashba coefficient, $\vec{k}$ is the momentum vector, $\vec{\sigma}$ is the Pauli matrix vector, and $\vec{z}$ is the unit vector along with the polar axis. In such a system, the Edelstein effect [18] is also observed, that is, a nonequilibrium spin accumulation occurs by applying an electric field to the spin-polarized bands. Thus, a highly efficient spin-to-charge conversion has been demonstrated in polar magnetic semiconductors [16] and interfacial systems [19–22]. Until now, no single phase, polar ferromagnetic metals have been observed at room temperature, although multilayers comprised of ferromagnets (e.g., Co/Pt [8,23]) can show polar magnetic metal behavior.

In van der Waals (vdW) systems, the stacking configuration can be engineered to manipulate crystal symmetry, for example by synthesis conditions [24], chemical doping [25], and external field [26], and thus it plays a crucial role in mediating physical phenomena such as ferroelectricity [27], magnetism [28], and superconductivity [29]. Recent work reported that capping a spin-orbit coupling layer on $Fe_3GeTe_2$ induces an interfacial DMI and skyrmions in this bilayer system below ambient temperature [30–33]. The $Fe_5GeTe_2$ system exhibits two-dimensional (2D) itinerant ferromagnetism with high Curie temperature, which provides an ideal platform to design such a metallic, polar magnetic material. The vdW $Fe_{5-x}GeTe_2$ magnet exhibits rhombohedral *ABC* stacking with a ferromagnetic ground state [34,35]. Interestingly, the introduction of cobalt into the iron sites within this compound has been shown to induce a structural phase transition to the inversion-centric, hexagonal *AA* stacked $(Fe_{1-y}, Co_y)_{5-x}GeTe_2$ ($y = 0.44, 0.46$) with an antiferromagnetic ordering [36,37]. Here, we report the experimental discovery of a hexagonally stacked $(Fe_{0.5}Co_{0.5})_5GeTe_2$ (FCGT) phase, denoted as $AA'$- stacked FCGT, by systematically increasing the cobalt doping to

*These authors contributed equally to this work.
†Corresponding author: hongruizhang@berkeley.edu
‡rramesh@berkeley.edu

 

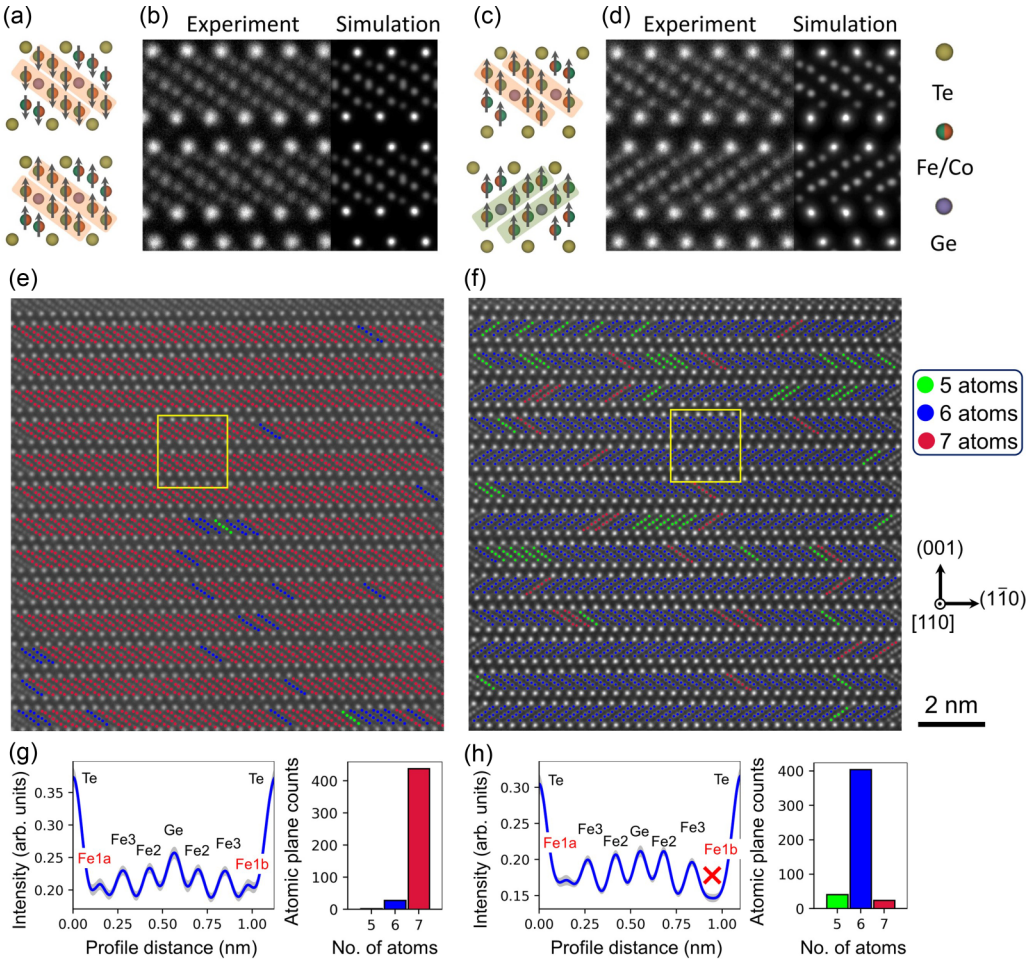


FIG. 1. Structural phase transition of $(Fe_{1-y}Co_y)_5GeTe_2$. (a)–(d) Structure model and corresponding HAADF-STEM cross-sectional images of FCGT for (a), (b) *AA* stacking ($y = 0.45$) and (c), (d) *AA′* stacking ($y = 0.50$) along the [110] direction. The black arrows represent the corresponding evolution of magnetic order and anisotropy. Enlarged experimental and corresponding simulated HAADF-STEM images of a 10-nm-thick FCGT for (b) *AA*-stacking and (d) *AA′*-stacking phases. (e), (f) The Fe-Co-Ge sublattices are color-coded by the number of atoms in the atomic planes, with 5(*G*), 6(*B*), and 7(*R*) atoms, respectively. The yellow boxes in (e), (f) indicate the regions for (b), (d), respectively. (g), (h) Te-Te intensity line profiles and the histograms show the counts for the number of atoms in each sublattice plane. The gray shaded area indicates the standard deviation of the intensity profiles.

50%. Distinct from the previously identified $Fe_NGeTe_2$ ($N = 3, 4, 5$) systems, the *AA′* stacked FCGT exhibits a polar crystal structure that shows ferromagnetic order with a remarkably high Curie temperature ($T_c$, $\sim$350 K). As a result of this polar structure, we observe a well-ordered lattice of Néel-type skyrmions at room temperature probed directly via Lorentz scanning transmission electron microscopy (L-STEM), magnetic force microscopy (MFM), and magneto-transport measurements. Spin torque ferromagnetic resonance (ST-FMR) and second-harmonic Hall measurement studies show a Rashba-Edelstein effect, illustrating the potential for use as both the ferromagnet and a spin-orbit torque metal in spintronic applications.

High-quality FCGT single crystals with the two different stacking symmetries were synthesized by tuning the cobalt concentration using a chemical vapor transport method (detail of the synthesis are presented in the Methods section in the Supplemental Material [38]). The composition of the FCGT platelets was confirmed by energy dispersive x-ray spectroscopy (EDS), illustrated for the 45% Co and 50% Co platelets (see the Supplemental Material, Fig. S1, for details [38]). Armed with the chemical stoichiometry, the atomic scale structure of these two platelets was studied. Pristine $Fe_5GeTe_2$ has an *ABC* stacking with a rhombohedral unit cell and space group $R\bar{3}m$ (No. 166) [36,37]; introduction of cobalt of up to 40–47 % atomic concentration transforms the FCGT crystal into the *AA* phase with the space group $P\bar{3}m1$ (No. 164) [36]. Surprisingly, as the cobalt concentration is increased to 50%, the *AA* stacked FCGT transitions into the *AA′* stacking, which belongs to the space group $P6_3mc$ (No. 186) (see the Methods section in the Supplemental Material, and single-crystal x-ray diffraction data in Figs. S2 and S3 for details [38]). This space group with a polar point group indicates that the *AA′* stacking FCGT is a unique noncentrosymmetric structure in the $Fe_NGeTe_2$ system ($N = 3, 4, 5$). To understand the atomistic origins of inversion symmetry in the *AA* and *AA′* phases, scanning transmission electron microscopy (STEM) was performed. Figure 1 illustrates

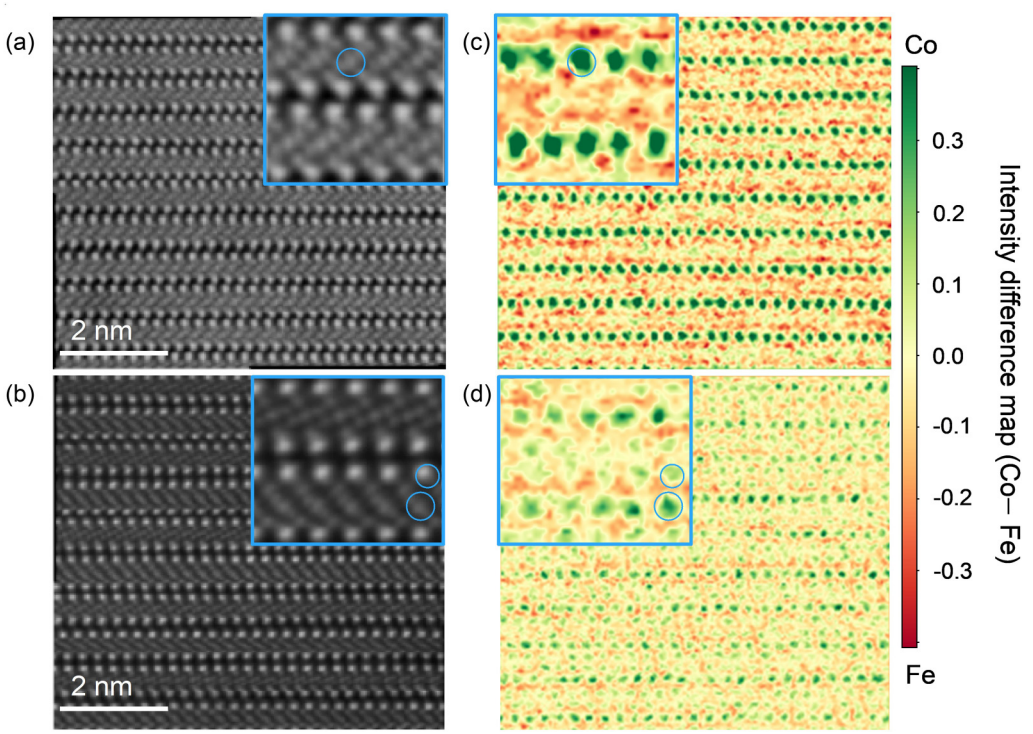


FIG. 2. Chemical distribution in FCGT. (a), (b) Simultaneous atomic resolution HAADF-STEM images for *AA* and *AA′* phase. (c), (d) Intensity difference EELS maps (Co-Fe) for *AA* and *AA′* phase. The inset indicates the zoomed-in images of the HAADF and EELS maps. Green coloring in the STEM-EELS maps indicates a relatively higher cobalt concentration, and orange coloring indicates a relatively higher iron concentration. The blue circles in the insets indicate the estimated delocalization radius of the EEL signal.

the atomic configuration for the two types of FCGT, labeled as *AA* [Fig. 1(a)] and *AA′* stacking [Fig. 1(c)]. High angle annular dark field–scanning transmission electron microscopy (HAADF-STEM) images of cross-sections in the [110] zone axis of the two platelets reveal strikingly different stacking information, shown in Figs. 1(b) and 1(d) and Figs. S4 and S5 (see the Supplemental Material for details [38]). The corresponding simulated images are shown to the right of the experimental images. The averaged intensity line traces for both of these images reveal a significant difference, as shown in Figs. 1(g) and 1(h). Both phases are built up of double Te layers between which the Fe/Co/Ge layers are stacked. The *AA* phase (45% Co) has a predominance of seven-layer stacking with a minority of six-layer stacking. In stark contrast, the *AA′* structure in the 50% Co sample has a predominance of six-layer stacks with a minority of five- and seven-layer stacks. It is also noteworthy that the three different Fe-sites (see the Supplemental Material, Fig. S3, for details [38]) are clearly not at the same intensity, hinting at the possibility of partial occupancy of these sites, particularly the Fe 1*a* and Fe 1*b* sites. This difference in stacking sequence between the two Te layers is captured at a larger scale in Figs. 1(e) and 1(f) for the *AA* and the *AA′* phases, respectively. These images are false-color coded to illustrate the differences in stacking sequence, which was derived from atomic columns that were Gaussian-fitted to extract their exact positions. The bar charts to the right of Figs. 1(g) and 1(h) summarize the statistics of the layer stacking for the *AA* and *AA′* phases. Thus, the Fe 1*a* sites ordering in the *AA′* phase FCGT break inversion symmetry, resulting in a net polar field along the *c* axis.

Armed with this atomic scale structural information, chemical mapping via simultaneous HAADF-STEM and electron energy loss spectroscopy (EELS) was performed. Details of the STEM-EELS acquisition parameters are described in the methods section of the text. EELS maps for the individual chemical species (i.e., Te, Fe, Co, and Ge) along with the ADF-STEM images are shown in Figs. S6 and S7 (see the Supplemental Material for details [38]), and exemplar individual EELS spectra are shown in Fig. S8 (see the Supplemental Material for details [38]). Figures 2(a) and 2(b) shows the simultaneously acquired atomic resolution HAADF images for *AA* and *AA′*, respectively, where we specifically focus on the Fe and Co EELS spectra. To distinguish between the atomic distribution of closely spaced (∼1.3 Å apart) Fe (red) and Co (green) atoms, we calculated the intensity difference maps by subtracting the normalized Co intensity from the normalized Fe intensity as shown in the maps in Figs. 2(c) and 2(d). The color scale used in the difference maps diverges from green to orange, where green indicates enrichment of Co while orange indicates Fe enrichment. The zoomed-in HAADF and EELS maps that are displayed as insets in Fig. 2 show the location of these Co enrichment sites. In the *AA* phase, Co enrichment is mostly limited to the Fe sites near the Ge atomic columns, i.e., Fe2 sites. However, in the *AA′* phase there are two Co sites that exhibit enrichment, namely Fe2, which is close to the Ge atoms, and Fe1, which is close to the Te atoms.

To provide insight into energetics of the centrosymmetric and polar phases of FCGT, density functional theory (DFT) calculations were performed using the exchange-correlation functional of Perdew, Burke, and Ernzerhof (PBE) [39] and

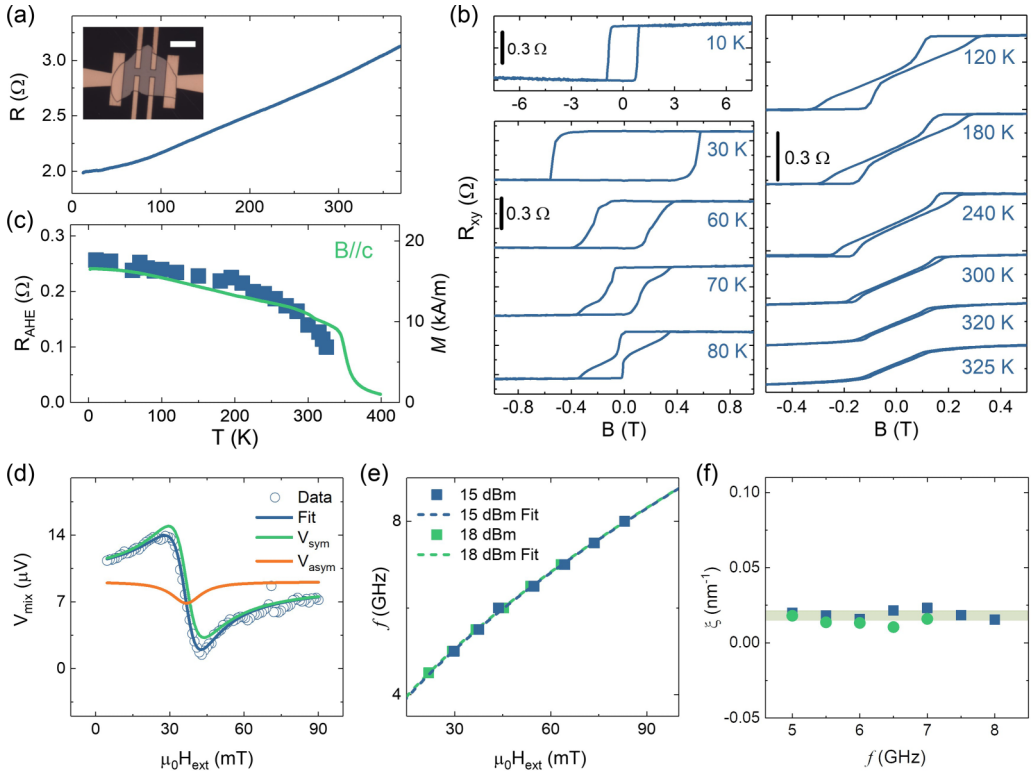


FIG. 3. Magnetotransport and ST-FMR measurements of $AA'$ phase FCGT nanoflakes. (a) Temperature dependence of the longitudinal resistance. The Hall bar device shown in the inset of (a) is based on a 200-nm-thick FCGT nanoflake on a $SiO_2$/Si substrate. The scale bar is 10 $\mu$m. (b) Hall resistance vs magnetic field at select temperatures. (c) Temperature dependence of the anomalous Hall resistance (blue square) in the saturation region. The temperature dependence of the magnetization (green line) was obtained at 5 mT. (d) The ST-FMR signal of an FCGT (21 nm, ∼11 unit cells)/$Co_{0.9}Fe_{0.1}$(12 nm) sample at 5.5 GHz, 18 dBm. The solid lines are fits that show the symmetric (orange) and antisymmetric (yellow) Lorentzian contribution. (e) ST-FMR frequency as a function of resonance field; the blue (15 dBm) and green (18 dBm) line is a fit to the Kittel formula. (f) Charge to spin conversion coefficient ($\xi$) (details in the Methods section in the Supplemental Material [38]) as a function of frequency at 15 and 18 dBm.

Hubbard U [40] and Grimme D3 van der Waals corrections [39] for the pristine stoichiometric end-point compounds $Fe_5GeTe_2$ and $Co_5GeTe_2$, assuming collinear magnetic order and a fixed Fe 1*a* site occupancy (details in the Methods section in the Supplemental Material [38]). The atomic positions and lattice parameters of $Fe_5GeTe_2$ and $Co_5GeTe_2$ for the *ABC*, *AA*, and *AA*′ phases with fixed Fe 1*a* site occupancies were optimized with DFT-PBE+U+D3 for both ferromagnetic and antiferromagnetic interplanar order. The ground-state energy per formula unit (f.u.) was computed from each relaxed geometry and appears in Table S1, along with details of each configuration's lattice parameters and magnetic order.

The DFT ground-state energies for *ABC*, *AA*, and *AA*′ structural and magnetic phases considered lie within about ±10 meV/f.u., strongly supporting the hypothesis that each relevant polytype is experimentally accessible. From the relaxed lattice parameters in Table S1, we identify a significant reduction of the out-of-plane *c* lattice parameter (1.7% for $Fe_5GeTe_2$ and 1.3% for $Co_5GeTe_2$) in the polar *AA*′ phase relative to the nonpolar *AA* and *ABC* structural phases for both Fe and Co compound species. This is consistent with the XRD measurements of the *AA*′ FCGT crystal (see the Supplemental Material, Figs. S2 and S3, for details [38]), which show a reduction in the *c* lattice parameter from *AA* to *AA*′ phases of similar composition. The computed intralayer spacings—i.e., the interplanar spacings of adjacent Fe/Co/Ge layers—for all relaxed structures and magnetic orders considered were calculated to be very similar for the different structural phases, with the *c* lattice parameter reduction largely resulting from a change in interlayer spacing—i.e., the vdW spacing between adjacent Te layers—unique to the *AA*′ phase. This reduction may also suggest that the distinct magnetic ordering behavior of this novel *AA*′ phase is influenced by a distance-sensitive interlayer exchange.

Temperature-dependent transport measurements of an *AA*′ phase FCGT nanoflake exhibit a typical metallic behavior [Fig. 3(a); the inset shows the Hall bar device], and the corresponding magnetic field dependence of the Hall resistance ($R_{xy}$) at various temperatures is shown in Fig. 3(b). At 10 K, $R_{xy}$ shows a rectangular hysteresis loop as a function of out-of-plane magnetic field, indicating a ferromagnetic ground state and a fully remnant, single magnetic domain state. At ∼70 K, the Hall data show a sheared out-of-plane hysteresis loop suggesting the onset of labyrinthine domains [41]. At higher temperatures (70–320 K), the sheared hysteresis loop remains while the saturation field gradually decreases. Finally, for temperatures higher than 325 K, the sheared hysteresis loops disappear. The value of $R_{AHE}$ is ∼0.25 Ω at 10 K, and the saturated $R_{AHE}$ in Fig. 3(b) decreases with increasing temperature,

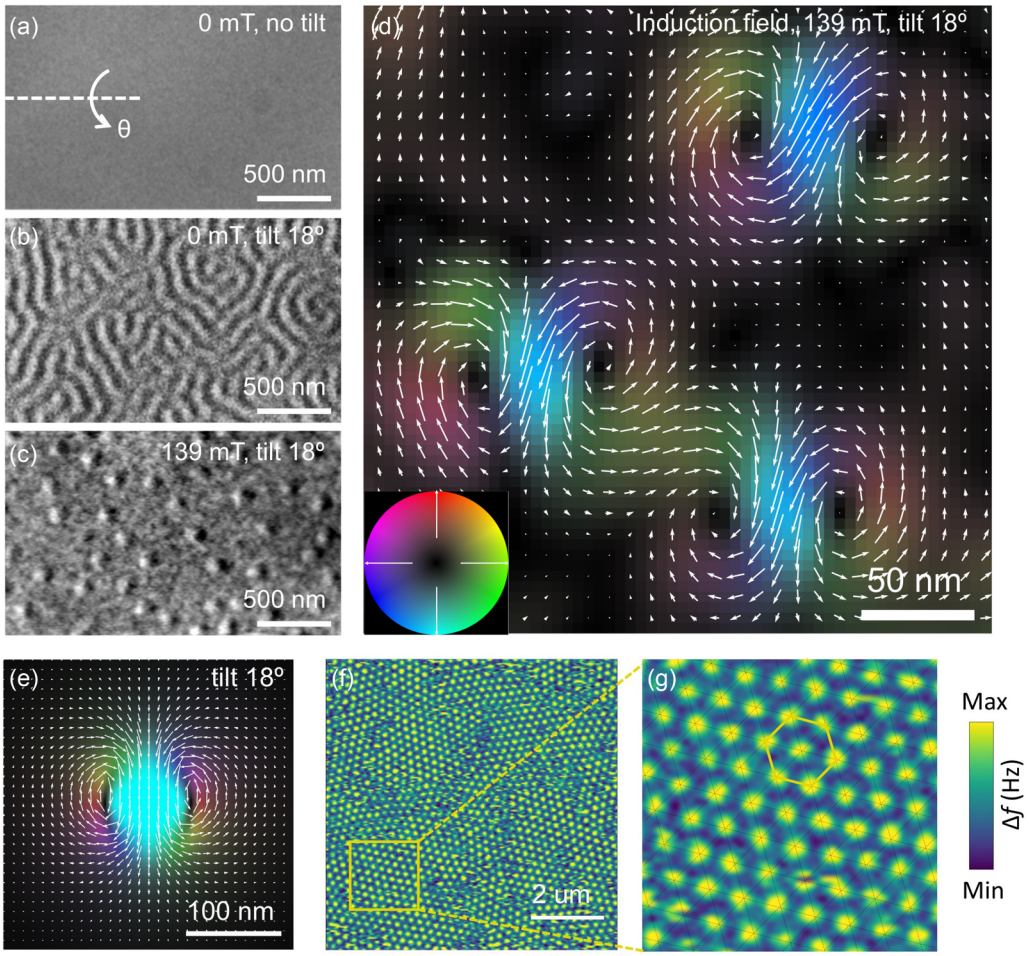


FIG. 4. Room temperature spin texture of $AA'$ phase FCGT. (a), (b) Lorentz TEM images of the 110-nm-thick nanoflake acquired at the same region under zero-field and +4 mm defocus with 0°-tilt and 18°-tilt reveal a labyrinth phase with Neél character. (c) In the same region at an 18°-tilt angle, isolated skyrmions emerge with an applied field of 139 mT. The skyrmion size is ∼90 nm, determined from the lateral distance between the minimum and maximum intensity profile of the bubbles. (d) Magnetic induction map obtained using four-dimensional Lorentz STEM (4D-LSTEM) equipped with an electron microscopy pixel array detector (EMPAD). The color and arrows indicate induction field components of Néel skyrmions perpendicular to the beam propagation direction for an 18° sample tilt. (e) Simulated magnetic induction map for a Neél skyrmion at an 18°-tilt. (f) MFM images of an FCGT nanoflake on a $SiO_2$/Si substrate. The thickness is ∼128 nm, obtained by the line profile of atomic force microscopy. (g) High magnification of the skyrmion lattice region indicated by the yellow box in (f). The skyrmion lattice parameter is ∼200 nm corresponding to a density of ∼23.3 skyrmions/$\mu$m$^2$.

revealing a surprisingly high $T_c$ of ∼350 K [Fig. 3(c)], which is consistent with the bulk magnetization measurements. The magnetotransport data along with the structural information in Fig. 1 establish $AA'$-stacked FCGT as a polar, magnetic metal.

Based on the experimental demonstrations of the unique structure and magnetic characteristic for $AA'$ phase FCGT, in the following the electrical and magnetic properties are presented. In wurtzite structure materials, due to the broken inversion symmetry, spin-orbit interaction causes splitting of the electronic band structure, leading to the Rashba effect. To verify such current-induced spin-orbit torques (SOTs) in the $AA'$ phase, we performed spin torque ferromagnetic resonance (ST-FMR) measurements on multiple samples at room temperature. A typical ST-FMR signal for an $AA'$-FCGT/$Co_{0.9}Fe_{0.1}$ sample is shown in Fig. 3(d); Fig. S12 (see the Supplemental Material for details [38]) shows details of the measurement. This spectrum can be fitted well to a sum of symmetric ($V_{sym}$) and asymmetric components ($V_{asym}$) (details in the Methods section in the Supplemental Material [38]), which are proportional to the in-plane dampinglike torque and out-of-plane torques, respectively. Figure 3(e) shows the ST-FMR frequency as a function of resonant field, which is in good agreement with the Kittel formula [42,43], leading to an effective magnetization of the $AA'$-FCGT/$Co_{0.9}Fe_{0.1}$ bilayer of 626 kA/m. The charge-to-spin conversion coefficient ($\xi$) as a function of frequency is essentially constant, as shown in Fig. 3(f). The average $\xi$ of the $AA'$-FCGT/$Co_{0.9}Fe_{0.1}$ system is $\sim 0.017 \pm 0.003\,\mathrm{nm}^{-1}$. In addition, an ST-FMR signal for an $AA$-FCGT/CoFe sample was also observed (see the Supplemental Material, Fig. S13, for details [38]) The average $\xi$ of $AA$-FCGT/$Co_{0.9}Fe_{0.1}$ is close to that of the $AA'$-FCGT/CoFe system. Due to the $AA$-FCGT without breaking inversion symmetry, this implies that the ST-FMR signal of the $AA'$-FCGT/$Co_{0.9}Fe_{0.1}$ sample may originate from the

Rashba-Edelstein effect of the $Te/Co_{0.9}Fe_{0.1}$ interface or the spin Hall effect from the FCGT system. To verify the existence of the bulk Rashba-Edelstein effect in this system, the second-harmonic Hall measurements were performed in the 100-nm-thick $AA'$ phase of a single-layer FCGT nanoflake (see the Supplemental Material, Fig. S14, for details [38]). The behavior we observed is similar to the result of the bulk magnetic Rashba system, Mn-doped GeTe [16]. By analysis, it gives a charge-to-spin conversion coefficient of $\xi \sim 0.024\,\mathrm{nm}^{-1}$. Even the second-harmonic Hall signal was observed in the single-layer $AA'$ FCGT. However, more approaches are still needed to distinguish the three contributions of the ST-FMR signal in detail in future work.

A polar magnet, which exhibits a sheared hysteresis loop, might be expected to form Néel-type skyrmions in finite external magnetic fields. To verify this, Lorentz TEM (LTEM) measurements were performed on the $AA'$ phase FCGT nanoflakes at room temperature to image the multidomain ground state. LTEM imaging was performed on a 110-nm-thick FCGT flake at a defocus of +4 mm at room temperature [Figs. 4(a)–4(c)]. At zero applied magnetic field, no magnetic contrast was observed at normal incidence [Fig. 4(a)]; labyrinthine domains are visible [Fig. 4(b)] once the sample is tilted by 18° around the horizontal imaging direction as indicated in Fig. 4(a). At zero tilt, the electron deflection cancels out due to the symmetric distribution of magnetization, and thus the images exhibit no contrast in the standard LTEM mode [44,45]. An external field applied in the LTEM along the beam direction triggers a domain morphology evolution from stripes to a mixture of bubbles and much shorter stripes (see the Supplemental Material, Fig. S15, for details [38]). When the magnetic field is increased up to 139 mT, we find that the bubbles clearly show dark/bright contrast perpendicular to the tilt axis, indicating Néel-type skyrmions [Fig. 4(c)]. Finally, when the magnetic field is increased to 160 mT, the sample is magnetically saturated into a single domain state.

To elucidate the detailed structure of such Néel-type skyrmions, four-dimensional LSTEM (4D-LSTEM) experiments were performed using a high-dynamic-range electron microscopy pixel array detector (EMPAD) [46]. 4D-LSTEM works by acquiring a full 2D, angle-resolved scattering distribution at each probe scanning position in a 2D grid, resulting in four-dimensional datasets. By quantitatively measuring the scattering distribution at each point in real space, 4D-LSTEM can detect the phase shift of the electron beam induced by the lateral magnetic induction field of the spin textures [Fig. 4(d)]. The magnetic induction field of Néel-type skyrmions [Fig. 4(d)] can thus be derived from the deflection of the electron beam in each diffraction pattern due to the Lorentz force, where the color and arrows represent the direction of the projected in-plane components [47]. A magnetic induction composed of clockwise and counterclockwise spin curls was observed, which agrees well with the calculated induction field distribution for Néel-type magnetic skyrmions, Fig. 4(e) and Fig. S16 (see the Supplemental Material for details [38]) [45,48]. The formation of skyrmions is also verified by magnetic force microscopy imaging illustrated in Figs. 4(f) and 4(g). We observe an ordered hexagonal skyrmion lattice at room temperature and zero field with a lattice parameter of ∼200 nm corresponding to a density of ∼23.3 skyrmions/$\mu m^2$. The zero-field skyrmion lattice is induced by the stray field of the MFM tips.

Based on these experimental demonstrations of skyrmions in the $AA'$ phase FCGT system, the physical origins of DMI are now discussed. The $AA'$ phase FCGT is a polar magnet with a $C_{6v}$ point group. The direction of effective DMI is perpendicular to the polar axis ($c$-axis), i.e., in-plane. Therefore, we carried out micromagnetic simulations to estimate the DMI constant at room temperature (see the section on methods in the Supplemental Material and Fig. S17 for details [38]). We simulated a 1 $\mu$m × 1 $\mu$m sample with a thickness of 110 nm, which is the same thickness as the sample imaged with LTEM. Given the simulation results, we found that as the DMI value increases, the domain pattern transitions from isolated skyrmions to a skyrmion lattice while its size decreases. By comparing the LTEM experimental results with the simulations, we estimated a value of the effective DMI constant of $\sim 0.95\,\mathrm{mJ/m^2}$.

The observation of a polar ferromagnetic metal at room temperature opens up exciting fundamental opportunities, with the potential to impact applications in spintronics. Our work clearly demonstrates the role of structural and chemical order, along with the subtle changes in electronic and spin structure through Co substitution, in triggering the broken inversion symmetry of the underlying crystal. This directly leads to the emergence of a bulk Dzyaloshinskii-Moriya coupling and Rashba-type spin-orbit coupling, which are fundamental requirements for both the formation of Néel-type skyrmions as well as the occurrence of a Rashba-Edelstein effect. This work shows enormous potential for crystal symmetry control of the spin and the electric quantum state of the materials.

H.Z., Y.T.S., J.R., and L.C. are supported by the Department of Defense, Air Force Office of Scientific Research under Award No. FA9550-18-1-0480. X.C, S.S., E.B.C, R.B., and R.R. acknowledge support by the U.S. Department of Energy, Office of Science, Office of Basic Energy Sciences, Materials Sciences and Engineering Division under Contract No. DE-AC02-05CH11231 with the Quantum Materials program (KC2202). R.C. and J.Y. acknowledge the support by Intel Corporation under an award titled Valleytronics center. L.C. acknowledges financial support from the University of California Office of the President and the Ford Foundation. X.H. is supported by the SRC-ASCENT center, which is part of the SRC-JUMP program. D.R. and P.F. are supported by the U.S. Department of Energy, Office of Science, Office of Basic Energy Sciences, Materials Sciences and Engineering Division under Contract No. DE-AC02-05-CH11231 (nonequilibrium magnetic materials program MSMAG). The electron microscopy studies were performed at the Cornell Center for Materials Research, a National Science Foundation (NSF) Materials Research Science and Engineering Centers program (DMR-1719875). The Cornell FEI Titan Themis 300 was acquired through NSF-MRI-1429155, with additional support from Cornell University, the Weill Institute, and the Kavli Institute at Cornell. The authors thank M. Thomas, J. G. Grazul, M. Silvestry Ramos, and K. Spoth for technical support and careful maintenance of the instruments. P.E. acknowledges funding by the Molecular Foundry, Lawrence

Berkeley National Laboratory, which is supported by the U.S. Department of Energy under Contract No. DE-AC02-05CH11231. The authors thank Rohan Dhall for FIB sample preparation. The devices were fabricated in the UC Berkeley Marvell Nanofabrication Laboratory. This research used the Lawrencium computational cluster resource provided by the IT Division at the Lawrence Berkeley National Laboratory, supported by the U.S. Department of Energy, Office of Science, Office of Basic Energy Sciences under Contract No. DE-AC02-05CH11231.

H.Z. and R.R. designed the experiments. X.C. and E B.C. synthesized the single crystals. X.C. did the EDS and magnetization measurements. N.S.S. and X.C. did the single crystal diffraction measurement. R.C. and J.Z. performed nanoflake preparation, sample transfer, and device fabrication. D.R. performed micromagnetic simulation. J.R. performed the *ab initio* calculations under the supervision of J.B.N. H.Z. and X.H. performed the Hall and ST-FMR measurements. H.Z. performed the AFM and MFM measurements. Y.T.S. and S.S. performed the STEM measurement with Z.C. and P.E. Y.T.S. performed the L(S)TEM measurements and simulation with Z.C. under the supervision of D.A.M. H.Z. and R.R. wrote the manuscript. All authors discussed results and commented on the manuscript.

[1] X. Z. Yu, Y. Onose, N. Kanazawa, J. H. Park, J. H. Han, Y. Matsui, N. Nagaosa, and Y. Tokura, Real-space observation of a two-dimensional skyrmion crystal, Nature (London) **465**, 901 (2010).

[2] K. Karube, J. S. White, N. Reynolds, J. L. Gavilano, H. Oike, A. Kikkawa, F. Kagawa, Y. Tokunaga, H. M. Ronnow, Y. Tokura, and Y. Taguchi, Robust metastable skyrmions and their triangular-square lattice structural transition in a high-temperature chiral magnet, Nat. Mater. **15**, 1237 (2016).

[3] C. Ciccarelli, L. Anderson, V. Tshitoyan, A. J. Ferguson, F. Gerhard, C. Gould, L. W. Molenkamp, J. Gayles, J. Železný, L. Šmejkal, Z. Yuan, J. Sinova, F. Freimuth, and T. Jungwirth, Room-temperature spin-orbit torque in NiMnSb, Nat. Phys. **12**, 855 (2016).

[4] S. Mühlbauer, B. Binz, F. Jonietz, C. Pfleiderer, A. Rosch, A. Neubauer, R. Georgii, and P. Böni, Skyrmion lattice in a chiral magnet, Science **323**, 915 (2009).

[5] P. Wadley, B. Howells, J. Železný, C. Andrews, V. Hills, R. P. Campion, V. Novák, K. Olejník, F. Maccherozzi, S. S. Dhesi, S. Y. Martin, T. Wagner, J. Wunderlich, F. Freimuth, Y. Mokrousov, J. Kuneš, J. S. Chauhan, M. J. Grzybowski, A. W. Rushforth, K. W. Edmonds, B. L. Gallagher, and T. Jungwirth, Electrical switching of an antiferromagnet, Science **351**, 587 (2016).

[6] X. Chen, S. Shi, G. Shi, X. Fan, C. Song, X. Zhou, H. Bai, L. Liao, Y. Zhou, H. Zhang, A. Li, Y. Chen, X. Han, S. Jiang, Z. Zhu, H. Wu, X. Wang, D. Xue, H. Yang, and F. Pan, Observation of the antiferromagnetic spin Hall effect, Nat. Mater. **20**, 800 (2021).

[7] R. Chen, F. Luo, Y. Liu, Y. Song, Y. Dong, S. Wu, J. Cao, F. Yang, A. N'Diaye, P. Shafer, Y. Liu, S. Lou, J. Huang, X. Chen, Z. Fang, Q. Wang, D. Jin, R. Cheng, H. Yuan, R. J. Birgeneau, and J. Yao, Tunable room-temperature ferromagnetism in Co-doped two-dimensional van der Waals ZnO, Nat. Commun. **12**, 3952 (2021).

[8] S. Woo, K. Litzius, B. Kruger, M. Y. Im, L. Caretta, K. Richter, M. Mann, A. Krone, R. M. Reeve, M. Weigand, P. Agrawal, I. Lemesh, M. A. Mawass, P. Fischer, M. Klaui, and G. S. Beach, Observation of room-temperature magnetic skyrmions and their current-driven dynamics in ultrathin metallic ferromagnets, Nat. Mater. **15**, 501 (2016).

[9] A. Fert, N. Reyren, and V. Cros, Magnetic skyrmions: Advances in physics and potential applications, Nat. Rev. Mater. **2**, 17031 (2017).

[10] O. Boulle, J. Vogel, H. Yang, S. Pizzini, D. de Souza Chaves, A. Locatelli, T. O. Mentes, A. Sala, L. D. Buda-Prejbeanu, O. Klein, M. Belmeguenai, Y. Roussigne, A. Stashkevich, S. M. Cherif, L. Aballe, M. Foerster, M. Chshiev, S. Auffret, I. M. Miron, and G. Gaudin, Room-temperature chiral magnetic skyrmions in ultrathin magnetic nanostructures, Nat. Nanotech. **11**, 449 (2016).

[11] I. Kezsmarki, S. Bordacs, P. Milde, E. Neuber, L. M. Eng, J. S. White, H. M. Ronnow, C. D. Dewhurst, M. Mochizuki, K. Yanai, H. Nakamura, D. Ehlers, V. Tsurkan, and A. Loidl, Neel-type skyrmion lattice with confined orientation in the polar magnetic semiconductor $GaV_4S_8$, Nat. Mater. **14**, 1116 (2015).

[12] T. Kurumaji, T. Nakajima, V. Ukleev, A. Feoktystov, T. H. Arima, K. Kakurai, and Y. Tokura, Neel-Type Skyrmion Lattice in the Tetragonal Polar Magnet $VOSe_2O_5$, Phys. Rev. Lett. **119**, 237201 (2017).

[13] Y. Fujima, N. Abe, Y. Tokunaga, and T. Arima, Thermodynamically stable skyrmion lattice at low temperatures in a bulk crystal of lacunar spinel $GaV_4Se_8$, Phys. Rev. B **95**, 180410(R) (2017).

[14] A. K. Srivastava, P. Devi, A. K. Sharma, T. Ma, H. Deniz, H. L. Meyerheim, C. Felser, and S. S. P. Parkin, Observation of robust Neel skyrmions in metallic PtMnGa, Adv. Mater. **32**, 1904327 (2020).

[15] K. Ishizaka, M. S. Bahramy, H. Murakawa, M. Sakano, T. Shimojima, T. Sonobe, K. Koizumi, S. Shin, H. Miyahara, A. Kimura, K. Miyamoto, T. Okuda, H. Namatame, M. Taniguchi, R. Arita, N. Nagaosa, K. Kobayashi, Y. Murakami, R. Kumai, Y. Kaneko, Y. Onose, and Y. Tokura, Giant Rashba-type spin splitting in bulk BiTeI, Nat. Mater. **10**, 521 (2011).

[16] R. Yoshimi, K. Yasuda, A. Tsukazaki, K. S. Takahashi, M. Kawasaki, and Y. Tokura, Current-driven magnetization switching in ferromagnetic bulk Rashba semiconductor (Ge,Mn)Te, Sci. Adv. **4**, eaat9989 (2018).

[17] A. Manchon, H. C. Koo, J. Nitta, S. M. Frolov, and R. A. Duine, New perspectives for Rashba spin-orbit coupling, Nat. Mater. **14**, 871 (2015).

[18] V. M. Edelstein, Spin polarization of conduction electrons induced by electric current in two-dimensional asymmetric electron systems, Solid State Commun. **73**, 233 (1990).

[19] I. Mihai Miron, G. Gaudin, S. Auffret, B. Rodmacq, A. Schuhl, S. Pizzini, J. Vogel, and P. Gambardella, Current-driven spin torque induced by the Rashba effect in a ferromagnetic metal layer, Nat. Mater. **9**, 230 (2010).

[20] E. Lesne, Y. Fu, S. Oyarzun, J. C. Rojas-Sánchez, D. C. Vaz, H. Naganuma, G. Sicoli, J. P. Attané, M. Jamet, E. Jacquet, J. M. George, A. Barthélémy, H. Jaffrès, A. Fert, M. Bibes, and L. Vila, Highly efficient and tunable spin-to-charge conversion through Rashba coupling at oxide interfaces, Nat. Mater. **15**, 1261 (2016).

[21] Q. Song, H. Zhang, T. Su, W. Yuan, Y. Chen, W. Xing, J. Shi, J. Sun, and W. Han, Observation of inverse Edelstein effect in Rashba-split 2DEG between $SrTiO_3$ and $LaAlO_3$ at room temperature, Sci. Adv. **3**, e1602312 (2017).

[22] H. Zhang, Y. Ma, H. Zhang, X. Chen, S. Wang, G. Li, Y. Yun, X. Yan, Y. Chen, F. Hu, J. Cai, B. Shen, W. Han, and J. Sun, Thermal spin injection and inverse Edelstein effect of the two-dimensional electron gas at EuO-$KTaO_3$ interfaces, Nano Lett. **19**, 1605 (2019).

[23] C. O. Avci, K. Garello, A. Ghosh, M. Gabureac, S. F. Alvarado, and P. Gambardella, Unidirectional spin Hall magnetoresistance in ferromagnet/normal metal bilayers, Nat. Phys. **11**, 570 (2015).

[24] L. M. Schneider, J. Kuhnert, S. Schmitt, W. Heimbrodt, U. Huttner, L. Meckbach, T. Stroucken, S. W. Koch, S. Fu, X. Wang, K. Kang, E.-H. Yang, and A. Rahimi-Iman, Spin-layer and spin-valley locking in CVD-grown AA′-and AB-stacked tungsten-disulfide bilayers, J. Phys. Chem. C **123**, 21813 (2019).

[25] D. Rhodes, D. A. Chenet, B. E. Janicek, C. Nyby, Y. Lin, W. Jin, D. Edelberg, E. Mannebach, N. Finney, A. Antony, T. Schiros, T. Klarr, A. Mazzoni, M. Chin, Y. C. Chiu, W. Zheng, Q. R. Zhang, F. Ernst, J. I. Dadap, X. Tong, J. Ma, R. Lou, S. Wang, T. Qian, H. Ding, R. M. Osgood Jr., D. W. Paley, A. M. Lindenberg, P. Y. Huang, A. N. Pasupathy, M. Dubey, J. Hone, and L. Balicas, Engineering the structural and electronic phases of $MoTe_2$ through W substitution, Nano Lett. **17**, 1616 (2017).

[26] S. Cho, S. Kim, J. H. Kim, J. Zhao, J. Seok, D. H. Keum, J. Baik, D.-H. Choe, K. J. Chang, K. Suenaga, S. W. Kim, Y. H. Lee, and H. Yang, Phase patterning for ohmic homojunction contact in $MoTe_2$, Science **349**, 625 (2015).

[27] Z. Fei, W. Zhao, T. A. Palomaki, B. Sun, M. K. Miller, Z. Zhao, J. Yan, X. Xu, and D. H. Cobden, Ferroelectric switching of a two-dimensional metal, Nature (London) **560**, 336 (2018).

[28] B. Huang, G. Clark, E. Navarro-Moratalla, D. R. Klein, R. Cheng, K. L. Seyler, D. Zhong, E. Schmidgall, M. A. McGuire, D. H. Cobden, W. Yao, D. Xiao, P. Jarillo-Herrero, and X. Xu, Layer-dependent ferromagnetism in a van der Waals crystal down to the monolayer limit, Nature (London) **546**, 270 (2017).

[29] E. Morosan, H. W. Zandbergen, B. S. Dennis, J. W. G. Bos, Y. Onose, T. Klimczuk, A. P. Ramirez, N. P. Ong, and R. J. Cava, Superconductivity in $Cu_xTiSe_2$, Nat. Phys. **2**, 544 (2006).

[30] Y. Wu, S. Zhang, J. Zhang, W. Wang, Y. L. Zhu, J. Hu, G. Yin, K. Wong, C. Fang, C. Wan, X. Han, Q. Shao, T. Taniguchi, K. Watanabe, J. Zang, Z. Mao, X. Zhang, and K. L. Wang, Néel-type skyrmion in $WTe_2/Fe_3GeTe_2$ van der Waals heterostructure, Nat. Commun. **11**, 3860 (2020).

[31] B. Ding, Z. Li, G. Xu, H. Li, Z. Hou, E. Liu, X. Xi, F. Xu, Y. Yao, and W. Wang, Observation of magnetic skyrmion bubbles in a van der Waals ferromagnet $Fe_3GeTe_2$, Nano Lett. **20**, 868 (2020).

[32] M. Yang, Q. Li, R. V. Chopdekar, R. Dhall, J. Turner, J. D. Carlström, C. Ophus, C. Klewe, P. Shafer, A. T. N'Diaye, J. W. Choi, G. Chen, Y. Z. Wu, C. Hwang, F. Wang, and Z. Q. Qiu, Creation of skyrmions in van der Waals ferromagnet $Fe_3GeTe_2$ on $(Co/Pd)_n$ superlattice, Sci. Adv. **6**, eabb5157 (2020).

[33] T. Xu, Z. Chen, H.-A. Zhou, Z. Wang, Y. Dong, L. Aballe, M. Foerster, P. Gargiani, M. Valvidares, D. M. Bracher, T. Savchenko, A. Kleibert, R. Tomasello, G. Finocchio, S.-G. Je, M.-Y. Im, D. A. Muller, and W. Jiang, Imaging the spin chirality of ferrimagnetic Néel skyrmions stabilized on topological antiferromagnetic $Mn_3Sn$, Phys. Rev. Mater. **5**, 084406 (2021).

[34] H. Zhang, R. Chen, K. Zhai, X. Chen, L. Caretta, X. Huang, R. V. Chopdekar, J. Cao, J. Sun, J. Yao, R. Birgeneau, and R. Ramesh, Itinerant ferromagnetism in van der Waals $Fe_{5-x}GeTe_2$ crystals above room temperature, Phys. Rev. B **102**, 064417 (2020).

[35] A. F. May, D. Ovchinnikov, Q. Zheng, R. Hermann, S. Calder, B. Huang, Z. Fei, Y. Liu, X. Xu, and M. A. McGuire, Ferromagnetism near room temperature in the cleavable van der Waals crystal $Fe_5GeTe_2$, ACS Nano **13**, 4436 (2019).

[36] A. F. May, M.-H. Du, V. R. Cooper, and M. A. McGuire, Tuning magnetic order in the van der Waals metal $Fe_5GeTe_2$ by cobalt substitution, Phys. Rev. Mater. **4**, 074008 (2020).

[37] C. Tian, F. Pan, S. Xu, K. Ai, T. Xia, and P. Cheng, Tunable magnetic properties in van der Waals crystals $(Fe_{1-x}Co_x)_5GeTe_2$, Appl. Phys. Lett. **116**, 202402 (2020).

[38] See Supplemental Material at http://link.aps.org/supplemental/10.1103/PhysRevMaterials.6.044403 for methods and additional analysis of structural and magnetic properties in the *AA* and *AA′* phase FCGT system.

[39] J. P. Perdew, K. Burke, and M. Ernzerhof, Generalized Gradient Approximation Made Simple, Phys. Rev. Lett. **77**, 3865 (1996).

[40] S. L. Dudarev, G. A. Botton, S. Y. Savrasov, C. J. Humphreys, and A. P. Sutton, Electron-energy-loss spectra and the structural stability of nickel oxide: An LSDA+U study, Phys. Rev. B **57**, 1505 (1998).

[41] Z. Fei, B. Huang, P. Malinowski, W. Wang, T. Song, J. Sanchez, W. Yao, D. Xiao, X. Zhu, A. F. May, W. Wu, D. H. Cobden, J. H. Chu, and X. Xu, Two-dimensional itinerant ferromagnetism in atomically thin $Fe_3GeTe_2$, Nat. Mater. **17**, 778 (2018).

[42] L. Liu, T. Moriyama, D. C. Ralph, and R. A. Buhrman, Spin-Torque Ferromagnetic Resonance Induced by the Spin Hall Effect, Phys. Rev. Lett. **106**, 036601 (2011).

[43] X. Huang, S. Sayed, J. Mittelstaedt, S. Susarla, S. Karimeddiny, L. Caretta, H. Zhang, V. A. Stoica, T. Gosavi, F. Mahfouzi, Q. Sun, P. Ercius, N. Kioussis, S. Salahuddin, D. C. Ralph, and R. Ramesh, Novel spin-orbit torque generation at room temperature in an all-oxide epitaxial $La_{0.7}Sr_{0.3}MnO_3/SrIrO_3$ system, Adv. Mater. **33**, 2008269 (2021).

[44] M. J. Benitez, A. Hrabec, A. P. Mihai, T. A. Moore, G. Burnell, D. McGrouther, C. H. Marrows, and S. McVitie, Magnetic microscopy and topological stability of homochiral Neel domain walls in a $Pt/Co/AlO_x$ trilayer, Nat. Commun. **6**, 8957 (2015).

[45] S. D. Pollard, J. A. Garlow, J. Yu, Z. Wang, Y. Zhu, and H. Yang, Observation of stable Neel skyrmions in cobalt/palladium

multilayers with Lorentz transmission electron microscopy, Nat. Commun. **8**, 14761 (2017).

[46] M. W. Tate, P. Purohit, D. Chamberlain, K. X. Nguyen, R. Hovden, C. S. Chang, P. Deb, E. Turgut, J. T. Heron, D. G. Schlom, D. C. Ralph, G. D. Fuchs, K. S. Shanks, H. T. Philipp, D. A. Muller, and S. M. Gruner, High dynamic range pixel array detector for scanning transmission electron microscopy, Microsc. Microanal. **22**, 237 (2016).

[47] M. Krajnak, D. McGrouther, D. Maneuski, V. O. Shea, and S. McVitie, Pixelated detectors and improved efficiency for magnetic imaging in STEM differential phase contrast, Ultramicroscopy **165**, 42 (2016).

[48] T. Denneulin, J. Caron, M. Hoffmann, M. Lin, H. K. Tan, A. Kovács, S. Blügel and R. E. Dunin-Borkowski, Off-axis electron holography of Néel-type skyrmions in multilayers of heavy metals and ferromagnets, Ultramicroscopy **220**, 113155 (2020).